

Probing Noncentrosymmetric 2D Materials by Fourier Space Second Harmonic Imaging

Lucas Lafeta,^{*,†} Sean Hartmann,[†] Bárbara Rosa,[‡] Stephan Reitzenstein,[‡]
Leandro M. Malard,^{*,¶} and Achim Hartschuh^{*,†}

[†]*Department of Chemistry and CeNS, LMU Munich, Butenandtstr. 5-13, 81377 Munich,
Germany.*

[‡]*Institute of Solid State Physics, Technische Universität Berlin, Hardenbergstraße 36, 10623
Berlin, Germany.*

[¶]*Departamento de Física, Universidade Federal de Minas Gerais, Av. Antônio Carlos 6627, Belo
Horizonte, Minas Gerais 30123-970, Brazil.*

E-mail: lucas.lafeta@cup.lmu.de; lmalard@fisica.ufmg.br; achim.hartschuh@lmu.de

Abstract

The controlled assembly of twisted 2D structures requires precise determination of the crystal orientation of their component layers. In the established procedure, the second-harmonic generation (SHG) intensity of a noncentrosymmetric layer is recorded while rotating the polarization of both the incident laser field and detected SHG, which can be time-consuming and tedious. Here, we demonstrate that the crystal orientation of transition metal dichalcogenides and hexagonal boron nitride can be directly determined by recording SHG images generated by tightly focused laser beams in Fourier space. Using an azimuthally polarized laser beam, the SHG image distinctly reflects the hexagonal structure of the crystal lattice, revealing its orientation quickly and accurately. This technique could significantly impact the field of twistronics, which studies the effects of the relative angle between the layers of a stacked 2D structure, as well as advance the nanofabrication of 2D materials.

The field of two-dimensional (2D) crystalline materials has seen a dramatic development within the last two decades. Apart from graphene, which is considered the first 2D material to be isolated, a vast number of other 2D materials exist, and this number continues expanding. In addition to their intriguing physical properties, these layered materials are ideally suited for forming stacked van der Waals (vdW) structures. The electro-optical properties of these structures are significantly influenced by the relative angle (twist) between the layers. This variable has proven crucial for numerous angle-dependent physical phenomena, leading to the emergence of the fields of twist-optics and twistrionics.^{1–18}

A key experimental challenge in this field is determining the crystal orientation of individual flakes^{19–22} while developing practical, fast, and precise techniques to achieve this. A widely used procedure for noncentrosymmetric materials is based on polarization-resolved detection of second-harmonic generation (SHG).^{23–26} This technique exploits the particular symmetry properties of the investigated materials and can be readily applied to a broad range of materials.^{27–36}

Within the 2D materials family semiconducting transition metal dichalcogenides (TMDs) have attracted particular interest because of their strong linear and nonlinear optical response, which stems from the large oscillator strength of tightly bound excitons.^{25,34,37–40} For this 2D materials class, SHG detection turned out to be a crucial and powerful tool for determining the number of layers in a given flake and its crystallographic orientation.^{25,34} Materials with a hexagonal crystalline structure, such as TMD monolayers (e.g. MoSe₂, WSe₂) and hexagonal boron nitride (h-BN), belong to the symmetry point group D_{3h} , for which only three of the 27 components of the second-order susceptibility tensor $\chi^{(2)}$ that determines the SHG response are nonzero.^{25,27,41} This crystalline symmetry translates into the following polarization dependence: If the input polarization matches the zigzag direction of the TMD (Fig. 1), the polarization of the emitted SHG is rotated by 90°. In contrast, input and output polarization directions are the same for input polarization parallel to the armchair direction. The crystal orientation is thus encoded in the polarization of the generated second harmonic response. In the established and broadly applied procedure for determining the crystal symmetries and crystallographic direction of 2D materials, the SHG inten-

sity is recorded while rotating the polarization of the incident laser field, together with polarization filtering of the generated SHG with respect to the fixed crystal orientation.^{25,34} Being a sequential and, hence, a time-consuming experiment may limit its use for fast orientational monitoring in applications such as multi-component 2D material assembly.

Here, we investigated SHG radiation patterns of 2D materials with D_{3h} symmetry in Fourier space. We find that in the case of a tightly focused Gaussian laser beam, the crystal orientation of the flakes can be derived from the ellipticity of the observed SHG patterns. A microscopic model that treats the SHG of the 2D material as a coherent superposition of the fields radiated by dipolar emitters within the area of the laser-illuminated layer and that considers the form of the $\chi^{(2)}$ tensor can quantitatively describe the detected patterns and their orientation dependence. For an azimuthally polarized laser beam in which the excitation polarization varies spatially, the detected SHG pattern directly reveals the hexagonal shape of the crystal lattice together with its orientation. The concept underlying this procedure is to encode polarization information into spatial information and leverage SHG's coherent nature. The approach presented provides a fast and precise tool for determining the crystal symmetry and orientation of a 2D material flake, a critical challenge in vdW multilayer structure assembly.

Fourier space SHG images of 2D materials

In this study, SHG from 2D materials on glass substrates is detected either in real or Fourier space. The setup is based on a confocal microscope with a high numerical aperture objective (NA = 1.3) (Fig. 1a, Supplementary Information Note 1). SHG images at 440 nm are recorded by a charge-coupled device (CCD) upon pulsed laser excitation at 880 nm. Fourier-space images that show the SHG radiation pattern, i.e., the angular distribution of SHG emission, are recorded in a conjugate back focal plane (BFP). Real-space images can be obtained by changing the focal length of the final focusing lens from f to $f/2$. Fig. 1b displays a representation of the crystallographic structure of a 2D monolayer with D_{3h} symmetry indicating zigzag and armchair directions. In the experiment,

monolayer flakes are localized and identified by raster scanning the sample while detecting the SHG light using an avalanche photodiode. A representative confocal SHG image of a MoSe₂ flake obtained in this way is included in Fig. 1c. The observed uniform SHG intensity confirms a spatially homogeneous monolayer flake. The general characterization of the samples is shown in Supplementary Information Note 2.

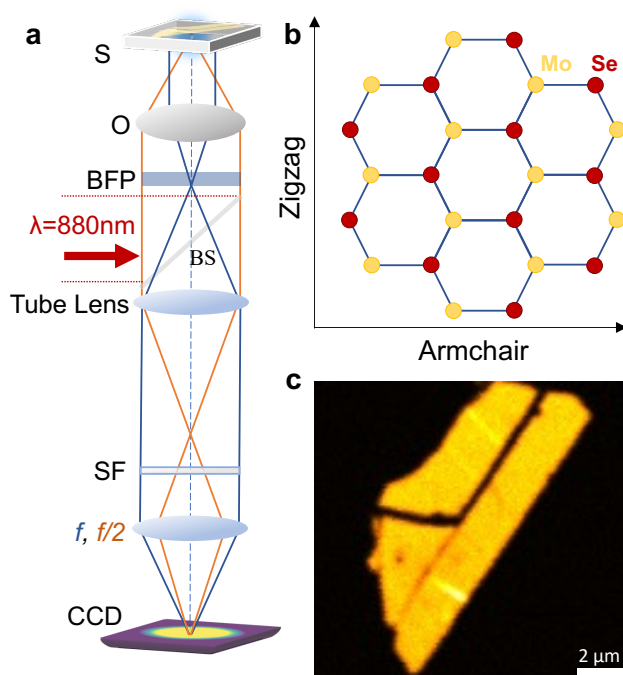


Figure 1: SHG imaging of 2D materials. **a** Microscope setup for the detection of real space and Fourier space (back focal plane, BFP) images. The fs-pulsed laser operating at 880 nm is directed to the objective (O) by a beam splitter (BS). The laser is focused on the sample, and the generated SHG at 440 nm is collected with the same objective, passing through a tube lens and a short pass filter (SF) to suppress the laser fundamental and detected by a CCD camera. Back focal plane imaging is done by placing a lens (known as Bertrand or Fourier lens) of focal length f (blue path), and real space imaging is done by a $f/2$ focal length lens (orange path). **b** Crystal structure of MoSe₂ 2D monolayers with D_{3h} symmetry. **c** Confocal SHG scan image of a MoSe₂ flake.

To understand the image contrast generated by nonlinear processes in 2D materials in Fourier space, we compare the results obtained for SHG with those for 2-photon excited photoluminescence (2PL), a nonlinear process that involves the simultaneous absorption of two photons.^{42,43} Fig. 2 presents the radiation patterns detected in Fourier space generated by 2PL and SHG obtained for a tightly focused Gaussian laser beam. The 2PL radiation pattern is radially symmet-

ric and features the highest intensities for angles above the critical angle θ_{crit} corresponding to $(k_x/k_0)^2 + (k_y/k_0)^2 \geq 1$ (Fig. 2a), where $k_{x,y}/k_0$ denote the in-plane wavevector components normalized by the wavevector in vacuum k_0 . The critical angle is determined by the ratio of the refractive indices of the glass/air interface according to $\sin \theta_{crit} = n_1/n_2$. Because 2PL is a spontaneous process, the 2PL radiation pattern can be represented by the sum of the intensities of the radiation patterns generated by incoherent point dipolar emitters excited within the illuminated sample area. Using the model described in Supplementary Information Note 3, the calculated pattern presented in Fig. 2b matches the experimental one without a free parameter. The observed radial symmetry indicates that the 2PL from MoSe₂ at room temperature is unpolarized. This can be accounted for in the model calculations using orthogonal in-plane dipoles.⁴⁴ In contrast, the SHG radiation pattern in Fig. 2c is most intense for $k_{x,y} = 0$ and slightly elliptical. Being a coherent process, SHG can be modeled as the sum of fields emitted by coherent dipoles, as shown in Fig. 2d, where a small ellipticity can be seen as well. In the model calculation, the strength of the dipolar emitters placed at different positions within the flake is scaled with the spatial intensity and polarization distribution in the exciting laser focus (refer to Methods section and Supplementary Information Note 3).

Observing the ellipticity in both the experimental and calculated SHG radiation patterns in Fig. 2, we explored its origin in detail starting with model calculations. For a single point dipole at a dielectric interface, the emission pattern directly reflects its orientation, with the maximum emission intensity occurring at angles greater than the critical angle (Fig. 2e).⁴⁵ For an extended illuminated area, on the other hand, the emitted SHG light can be calculated as a coherent superposition of the fields radiated by a spatial distribution of dipoles (Fig. 2g).³³ In this large area limit, i.e. with area dimensions exceeding the wavelength of the emitted light, the radiation pattern becomes a radially symmetric peak due to destructive interference of large angle contributions. Importantly, the resulting pattern contains no information on the orientation of the emitting dipoles. For a tightly focused laser beam and a correspondingly narrow distribution of emitting dipoles, however, the calculated radiation pattern retains polarization information in the form of an ellipse

oriented perpendicular to the direction of the emitting dipoles⁴⁶ (Fig. 2f). Although the orientation of this ellipse would enable us to determine the polarization of the emitted SHG light directly from Fourier images and thus infer the crystal orientation, a secondary contribution to the ellipticity of the detected pattern arises, which can partially offset the first.

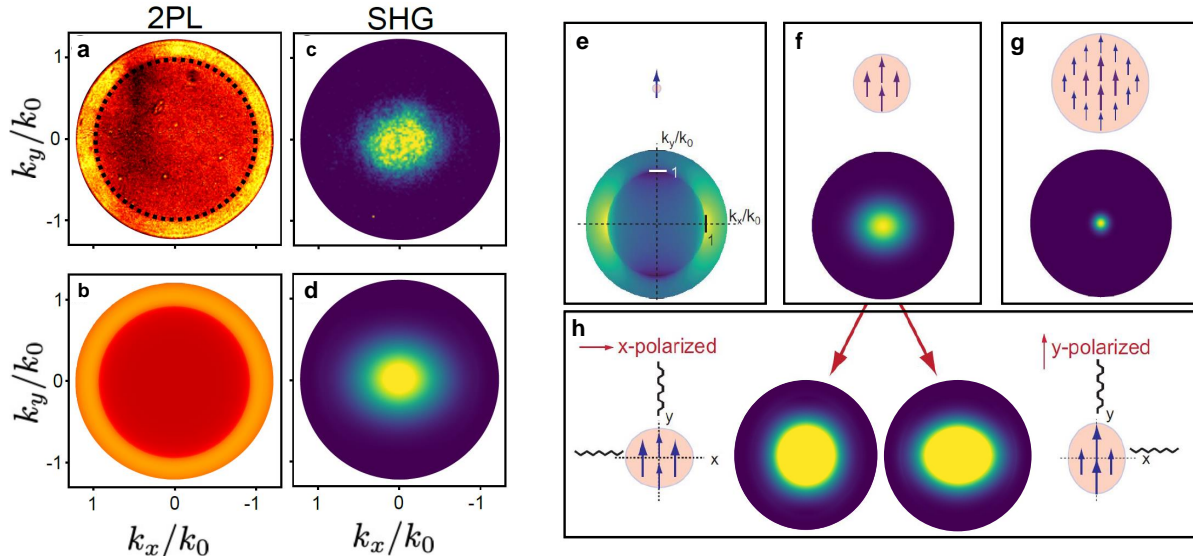


Figure 2: Origin of the ellipticity of SHG radiation patterns. Experimental radiation patterns generated by 2PL in **a** and SHG in **c** were detected in the BFP. The dashed circle in **a** denotes $(k_x/k_0)^2 + (k_y/k_0)^2 = 1$. **b** Calculated radiation pattern from the sum of incoherent point dipoles with isotropic in-plane orientation. **d** Calculated pattern for coherent point dipoles oriented in the x-direction (see text and Methods section). **e - g** Calculated radiation patterns generated by an increasing number of coherent point dipoles oriented in the x-direction. The red-shaded circles represent the laser-illuminated focal area. The radiation pattern of a single point dipole (left) features characteristic emission lobes for $(k_x/k_0)^2 + (k_y^2/k_0) > 1$. No oriental information is contained in the circular pattern for weak focusing (right). For a tightly focused Gaussian laser beam (middle) with full-width at half maximum (FWHM) = 405 nm, information on the dipole orientation is retained in the form of an elliptical emission pattern. **h** For both incident polarization parallel to the zigzag axis (x-polarized) and parallel to the armchair axis (y-polarized), the resulting SHG emission is polarized in y-direction. A tightly focused Gaussian laser beam features an elliptical intensity distribution with the long axis parallel to the laser polarization (red-shaded ellipses). This reduces the ellipticity of the SHG pattern for incident polarization parallel to the zigzag axis (left pattern) and enhances it for armchair polarization (right pattern). Note that the radiation patterns are observed in Fourier space, such that the long and short axis of the red-shaded areas appear inverted. The color scale was saturated for better visualization of ellipticity.

For a tightly focused x-polarized Gaussian laser mode, the distribution of the x-component of the electric field is elliptical due to the different projections of the p- and s-polarized fields onto

the x-y-plane (Fig. 2h).⁴⁷ Hence, the in-plane intensity distribution of the generated SHG light in real space becomes elliptical, which translates into an additional contribution to the ellipticity of the radiation pattern that follows the polarization of the incident field. As a result, the ellipticity of the pattern obtained for laser polarization parallel to the armchair axis (y-polarized in Fig. 2h) is increased compared to that for laser polarization parallel to the zigzag axis. For polarization angles between x-and y-polarization, both ellipticity and the orientation of the ellipse vary gradually. In summary, the ellipse's orientation and ellipticity result from the interplay between the radiation pattern of a narrow emitting focal area, the nonlinear susceptibility tensor of noncentrosymmetric 2D materials that determine the polarization of the emitted SHG light, and the field distribution of a tightly focused laser beam.

Crystal orientation from Fourier SHG patterns

To validate the model predictions for the polarization angle-dependent Fourier SHG patterns made above, we measured the Fourier SHG images generated by a MoSe₂ monolayer with known orientation while rotating the polarization of the incident Gaussian laser beam. As can be seen in Fig. 3 for images taken every 30° both ellipticity and ellipse orientation vary in good agreement with the calculated patterns using the coherent dipole model described in the Methods section. The experimentally derived ellipticities are shown below in Fig. 5b together with the calculated ones and the 6-fold intensity pattern using the established technique based on synchronously rotating incident laser polarization and detection polarization of the SHG light²⁵ (Fig. 5a). We can see that the ellipticity indeed follows the same dependence on input polarization. Importantly, the quantitative agreement with the calculated values shows that the ellipticity provides a direct measure of the crystal orientation in contrast to the intensity-based technique which involves sequential measurements. However, the ellipticity-based technique requires careful optical alignment and data analysis. A more robust and direct approach is presented in the next section using an azimuthally polarized laser mode.

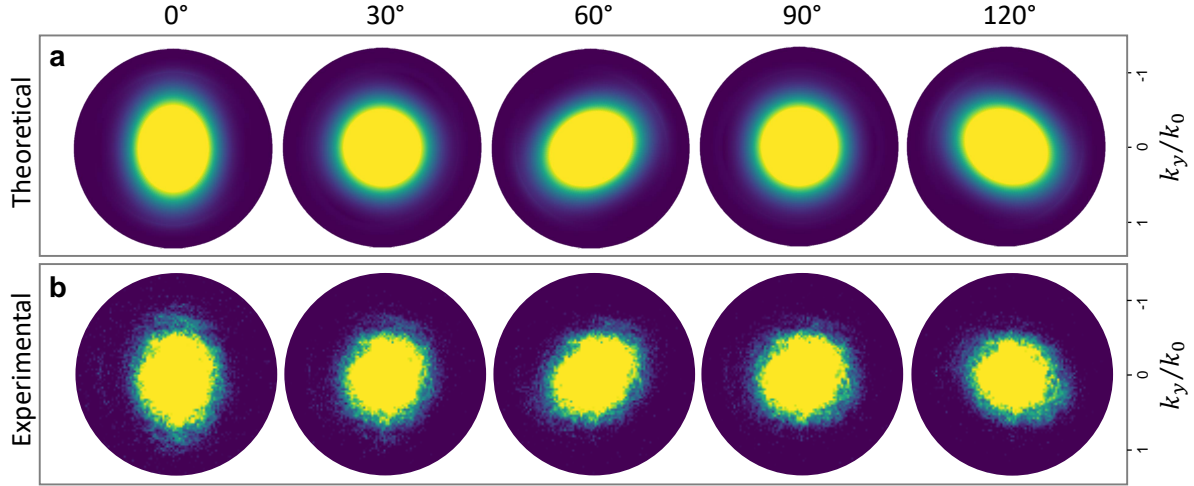


Figure 3: Excitation polarization dependence of SHG radiation patterns. **a** Calculated SHG radiation patterns for D_{3h} symmetry upon increasing the angle of the incident laser polarization with respect to the fixed directions of the crystallographic axis. **b** Experimental SHG radiation patterns for the corresponding incident laser polarizations using MoSe₂ monolayer.

Fourier SHG images using azimuthally polarized laser mode

In the previous section, we derived information on the polarization direction of the SHG light by carefully studying its influence on the observed Fourier SHG images. Now, we follow a different approach and encode polarization information into the spatial coordinates of the exciting laser field in the form of an azimuthally polarized laser beam (Fig. 4a). Depending on the local orientation of the input focal field relative to the armchair and zigzag directions, respectively, the SHG retains the polarization direction of the excitation light or appears rotated by 90°. The resulting field distribution of the SHG light reflects this complex interplay (Fig. 4b). This field distribution then translates into the observed radiation pattern. Fig. 4c presents the simulation results for the Fourier SHG image, and Fig. 4d the experimental result for a MoSe₂ monolayer. Both patterns show the highest intensities around the critical angle (NA=1) and feature the 6-fold symmetry of the underlying crystal lattice.

To further confirm the correlation between the SHG radiation pattern and the crystal lattice orientation, we recorded confocal SHG images of the MoSe₂ flake to determine its orientation before

and after rotation, using the observable edges of the flake as reference. Fig. 4e and f show the flake at an initial orientation of 102° with respect to the horizontal and after rotation at 8° , respectively. The corresponding radiation patterns in Fig. 4g, h reflect this rotation. As demonstrated in Supplementary Information Note 4, Fourier SHG detection using an azimuthal laser beam enables the discrimination of rotation angles smaller than $\sim 0.5^\circ$ with SHG image acquisition times of 1 second. In Fig. 5c, we show the intensity extracted along the red circular curve in Fig. 6 obtained for monolayer MoSe_2 together with the fit result using the formula described in Supplementary Information Note 4. The observed angle dependence matches those obtained by polarization-resolved SHG (Fig. 5a) and ellipticity measurements (Fig. 5b) discussed above, which were recorded for the same flake and orientation.

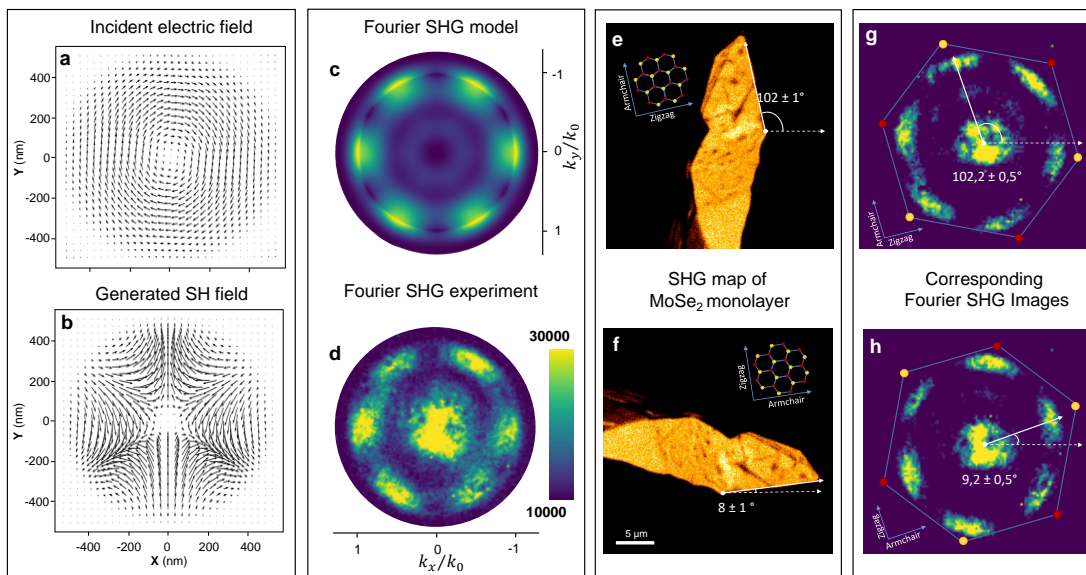


Figure 4: Fourier SHG images for azimuthal mode excitation show the crystallographic orientation. **a** Focal field distribution of the incident azimuthal polarization mode. **b** Focal field distribution of the SH generated by the D_{3h} symmetry material. Fourier SHG images using azimuthal mode **c** model and **d** experiment, revealing the hexagonal structure of the material. **e-h** Confocal SHG and Fourier SHG images of a MoSe_2 flake before (**e**, **g**) and after rotation by $\sim 90^\circ$ (**f**, **h**), respectively.

Additionally, we find a similar 6-fold pattern in the real-space SHG image, though it exhibits a strong dependence on defocusing, as demonstrated in Supplementary Information Note 5. For

practical purposes, Fourier SHG patterns are far more useful because they retain their symmetry properties and orientation even under significant defocus conditions. The signal contribution in the center of the experimental patterns in Fig. 4 d,g,h, and Fig. 6 indicate incomplete destructive interference of SHG generated at different positions within the focus, which could be due to deviations from pure azimuthal laser polarization, sample roughness and crystallographic disorder.

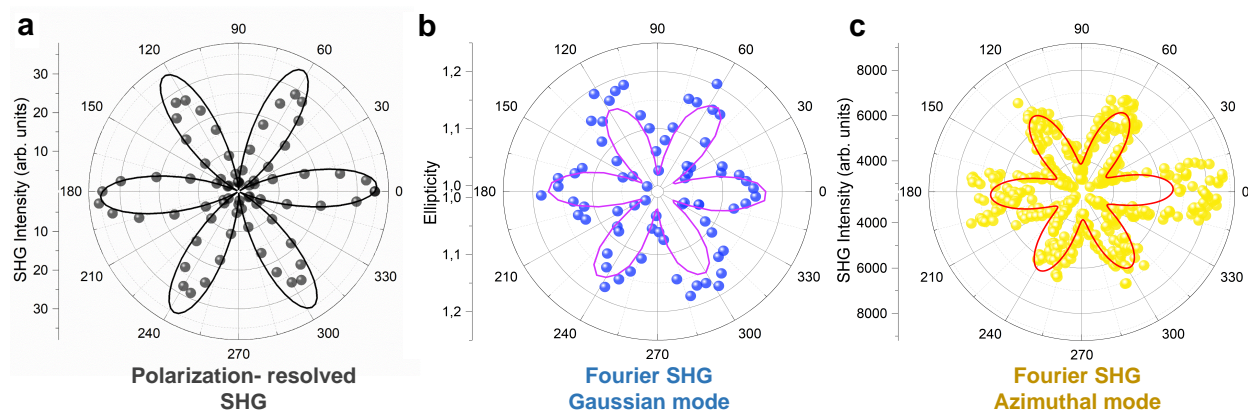


Figure 5: Comparison of techniques for determining crystal orientation. **a** SHG intensity as a function of the angle between the crystal armchair axis and the incoming and outgoing light polarization for a MoSe₂ monolayer sample. The circles are the experimental data, while the black line is the theoretical six-fold SHG intensity pattern. **b** Ellipticity of the detected SHG radiation pattern as a function of incoming light polarization relative to the armchair axis. The blue circles are extracted from the experimental data, while the violet line is from the model calculations. **c** Plot polar of the intensity of Fourier SHG pattern using the azimuthal mode. The red line is the fit using the equation of Supplementary Information Note 4. The yellow circles are the intensity of the SHG extracted along the red circle of the MoSe₂ monolayer in Fig. 6 below.

In addition to MoSe₂, Fig. 6 presents azimuthal mode Fourier SHG images of WSe₂ and h-BN, which exhibit the same 6-fold patterns, reflecting their D_{3h} symmetry and respective orientations. A detailed sequence of measurements recording the 6-fold pattern using polarisation-resolved SHG and the Fourier SHG ellipticities for the samples shown in Fig. 6 can be found in Supplementary Information Video 1. The presented data thus confirms the general applicability of the presented approach to other materials with D_{3h} symmetry.

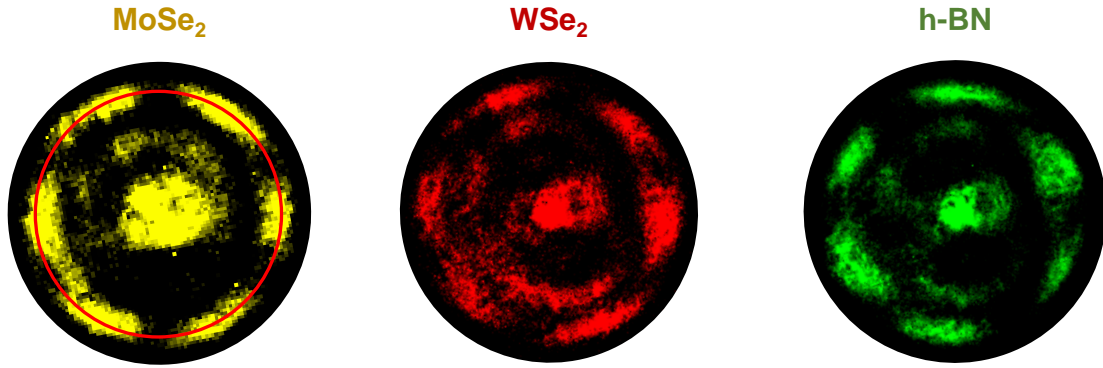


Figure 6: Azimuthal mode Fourier SHG images of different D_{3h} materials. Fourier SHG pattern using the azimuthal mode for MoSe₂ (yellow), WSe₂ (red), and h-BN (green). A series of measurements for the samples presented in **d** is included in .

CONCLUSION

In summary, we demonstrated that Fourier space SHG imaging of noncentrosymmetric 2D materials enables the retrieval of information about the symmetry and orientation of their crystal lattice. We first investigated the SHG radiation patterns obtained for a tightly focused Gaussian laser beam. We found a complex interplay between the excitation field’s elliptical distribution and the radiation pattern’s ellipticity created by a coherent superposition of dipolar SHG emitters in the focus generating the second harmonic light. The resulting ellipticity of the SHG Fourier patterns allows for the retrieval of the crystal orientation and provides a test case for the developed microscopic model that describes SHG image formation. However, the underlying procedure is experimentally demanding and, therefore, less practical.

We proposed and implemented a more direct approach using an azimuthally polarized laser beam, which encodes polarization information in the spatial coordinates of the excitation field. The recorded Fourier SHG images directly reflect the crystal lattice symmetry and its orientation, which can be described quantitatively by our model calculations. We further note that the approach could also be used to investigate other noncentrosymmetric materials by explicitly considering the crystal symmetry through the associated second-order nonlinear susceptibility tensor. The presented approach provides a rapid and precise tool that could readily be incorporated into

nanofabrication procedures for the assembly of twisted 2D material and materials characterization in general.

METHODS

SHG imaging map and BFP detection

Experiments were performed on the confocal microscope setup illustrated in Fig. 1 a and in Supplementary Information Note 1. For SHG and 2PL experiments, we use a femtosecond pulsed laser source operating at 880 nm.⁴⁸ Silver mirrors guided the beam to an inverted microscope after being reflected by a non-polarising beamsplitter and focused by a NA=1.3 immersion oil objective onto the sample. Generated SHG and 2PL were collected by the same objective and spectrally filtered using a short pass and a band pass filter centered at 440 nm in the case of SHG, and an 850 nm short pass and a 600 nm long pass filter for 2PL. BFP patterns were measured using a CCD camera. Fourier and real space imaging modes are switched by exchanging the final lens with a lens with half the focal length. The samples are mapped on a scanning unit while the light is detected by a sensitive avalanche photodiode (APD). To record polarization-dependent SHG intensities, we rotated the incident Gaussian beam with a half-wave plate in the input beam path parallel to a polarizer in the detection beam path. Fourier space SHG images are detected without a polarizer in the detection beam path. The azimuthal laser beam was generated using a laser mode converter.

Preparation of 2D materials

Using commercial bulk crystals, we performed mechanical exfoliation⁴⁹ onto polydimethylsiloxane (PDMS) stamp to thin down the TMD multi-flakes. Monolayers were identified by optical contrast imaging. The selected monolayers were transferred onto 160 μm glass cover slides at 70 °C by the dry-transfer method.⁵⁰ Bright field contrast images, photoluminescence spectra and confocal SHG maps are included in Supplementary Information Note 2.

Modelling of SHG images The incident field distributions of focused laser beams can be calculated analytically as described, for example, by Hecht *et al.*⁴⁷ In the calculations, the inci-

dent field is first projected onto the crystal axis, where the x-direction is taken to be parallel to a zigzag direction of the crystal lattice (Fig. 1b). The induced polarization at the second harmonic $P = (P_x, P_y, 0)$ is then calculated as $P_x = 2E_x E_y$ and $P_y = E_x^2 - E_y^2$ where E_x (E_y) is the incident electrical field component parallel (perpendicular) to the zigzag (armchair) direction. Due to symmetry reasons, only three components of the second-order susceptibility tensor $\chi^{(2)}$ are nonzero with in-plane polarization. As can be seen for incident field polarization parallel to the zigzag axis, the SHG polarization is rotated by 90° . In contrast, the polarization direction remains unaffected for incident polarization parallel to the armchair direction. The Fourier SHG radiation pattern detected in the back-focal plane of the microscope objective is then calculated as the coherent sum of the radiation patterns generated by point dipoles as described in ref. 45 in the illuminated sample area weighted by the local field distribution $(E_x(x, y), E_y(x, y))$ of the strongly focused laser beam. A propagation factor of $f(x, y, \phi, \theta) = \exp(-ik_1(x \cos(\phi) \sin(\theta) + y \sin(\phi) \sin(\theta)))$ accounts for retardation. Here, k_1 denotes the wavevector in the glass substrate, ϕ the in-plane orientation of the emitting dipole, and θ the angle of the emitted wave relative to the optical axis. From the Fourier space pattern, the corresponding real space image is calculated using the integral forms in ref. 47 (Supplementary Information Note 3).

REFERENCES

- (1) Li, E.; Hu, J.-X.; Feng, X.; Zhou, Z.; An, L.; Law, K. T.; Wang, N.; Lin, N. Lattice reconstruction induced multiple ultra-flat bands in twisted bilayer WSe_2 . *Nat. Commun.* **2021**, *12*, 5601.
- (2) Yankowitz, M.; Chen, S.; Polshyn, H.; Zhang, Y.; Watanabe, K.; Taniguchi, T.; Graf, D.; Young, A. F.; Dean, C. R. Tuning superconductivity in twisted bilayer graphene. *Science* **2019**, *363*, 1059–1064.
- (3) Ciarrocchi, A.; Tagarelli, F.; Avsar, A.; Kis, A. Excitonic devices with van der Waals heterostructures: valleytronics meets twistronics. *Nat. Rev. Mater.* **2022**, *7*, 449–464.

- (4) Förg, M.; Baimuratov, A. S.; Kruchinin, S. Y.; Vovk, I. A.; Scherzer, J.; Förste, J.; Funk, V.; Watanabe, K.; Taniguchi, T.; Högele, A. Moiré excitons in MoSe₂-WSe₂ heterobilayers and heterotrilayers. *Nat. Commun.* **2021**, *12*, 1656.
- (5) Arora, H. S.; Polski, R.; Zhang, Y.; Thomson, A.; Choi, Y.; Kim, H.; Lin, Z.; Wilson, I. Z.; Xu, X.; Chu, J.-H.; Watanabe, K.; Taniguchi, T.; Alicea, J.; Nadj-Perge, S. Superconductivity in metallic twisted bilayer graphene stabilized by WSe₂. *Nature* **2020**, *583*, 379–384.
- (6) Tarnopolsky, G.; Kruchkov, A. J.; Vishwanath, A. Origin of Magic Angles in Twisted Bilayer Graphene. *Phys. Rev. Lett.* **2019**, *122*, 106405.
- (7) Carr, S.; Massatt, D.; Fang, S.; Cazeaux, P.; Luskin, M.; Kaxiras, E. Twistronics: Manipulating the electronic properties of two-dimensional layered structures through their twist angle. *Phys. Rev. B* **2017**, *95*, 075420.
- (8) Devakul, T.; Crépel, V.; Zhang, Y.; Fu, L. Magic in twisted transition metal dichalcogenide bilayers. *Nat. Commun.* **2021**, *12*, 6730.
- (9) Shabani, S.; Halbertal, D.; Wu, W.; Chen, M.; Liu, S.; Hone, J.; Yao, W.; Basov, D. N.; Zhu, X.; Pasupathy, A. N. Deep moiré potentials in twisted transition metal dichalcogenide bilayers. *Nat. Phys.* **2021**, *17*, 720–725.
- (10) Wu, F.; Lovorn, T.; Tutuc, E.; Martin, I.; MacDonald, A. Topological Insulators in Twisted Transition Metal Dichalcogenide Homobilayers. *Phys. Rev. Lett.* **2019**, *122*, 086402.
- (11) Andersen, T. I. et al. Excitons in a reconstructed moiré potential in twisted WSe₂/WSe₂ homobilayers. *Nat. Mater.* **2021**, *20*, 480–487.
- (12) Sung, J. et al. Broken mirror symmetry in excitonic response of reconstructed domains in twisted MoSe₂/MoSe₂ bilayers. *Nat. Nanotechnol.* **2020**, *15*, 750–754.
- (13) Weston, A. et al. Atomic reconstruction in twisted bilayers of transition metal dichalcogenides. *Nat. Nanotechnol.* **2020**, *15*, 592–597.

- (14) Enaldiev, V.; Zólyomi, V.; Yelgel, C.; Magorrian, S.; Fal'ko, V. Stacking Domains and Dislocation Networks in Marginally Twisted Bilayers of Transition Metal Dichalcogenides. *Phys. Rev. Lett.* **2020**, *124*, 206101.
- (15) Scuri, G. et al. Electrically Tunable Valley Dynamics in Twisted WSe₂/WSe₂ Bilayers. *Phys. Rev. Lett.* **2020**, *124*, 217403.
- (16) Xu, Y.; Kang, K.; Watanabe, K.; Taniguchi, T.; Mak, K. F.; Shan, J. A tunable bilayer Hubbard model in twisted WSe₂. *Nat. Nanotechnol.* **2022**, *17*, 934–939.
- (17) Li, G.; Luican, A.; Lopes dos Santos, J. M. B.; Castro Neto, A. H.; Reina, A.; Kong, J.; Andrei, E. Y. Observation of Van Hove singularities in twisted graphene layers. *Nat. Phys.* **2010**, *6*, 109–113.
- (18) Gadelha, A. C. et al. Localization of lattice dynamics in low-angle twisted bilayer graphene. *Nature* **2021**, *590*, 405–409.
- (19) Mak, K. F.; Shan, J. Semiconductor moiré materials. *Nat. Nanotechnol.* **2022**, *17*, 686–695.
- (20) Kapfer, M. et al. Programming twist angle and strain profiles in 2D materials. *Science* **2023**, *381*, 677–681.
- (21) Wang, W. et al. Clean assembly of van der Waals heterostructures using silicon nitride membranes. *Nat. Electron.* **2023**, *6*, 981–990.
- (22) Liao, M. et al. Precise control of the interlayer twist angle in large scale MoS₂ homostructures. *Nat. Commun.* **2020**, *11*, 2153.
- (23) Psilodimitrakopoulos, S.; Mouchliadis, L.; Paradisanos, I.; Lemonis, A.; Kioseoglou, G.; Stratakis, E. Ultrahigh-resolution nonlinear optical imaging of the armchair orientation in 2D transition metal dichalcogenides. *Light. Sci. Appl.* **2018**, *7*, 18005–18005.
- (24) Autere, A.; Jussila, H.; Dai, Y.; Wang, Y.; Lipsanen, H.; Sun, Z. Nonlinear Optics with 2D Layered Materials. *Adv. Mater.* **2018**, *30*, 1705963.

- (25) Li, Y.; Rao, Y.; Mak, K. F.; You, Y.; Wang, S.; Dean, C. R.; Heinz, T. F. Probing Symmetry Properties of Few-Layer MoS₂ and h-BN by Optical Second-Harmonic Generation. *Nano Lett.* **2013**, *13*, 3329–3333.
- (26) Ma, H.; Liang, J.; Hong, H.; Liu, K.; Zou, D.; Wu, M.; Liu, K. Rich information on 2D materials revealed by optical second harmonic generation. *Nanoscale* **2020**, *12*, 22891–22903.
- (27) Boyd, R. W. In *Nonlinear Optics (Third Edition)*; Boyd, R. W., Ed.; Academic Press: Burlington, 2008; pp 1–67.
- (28) Shen, Y. R. Optical Second Harmonic Generation at Interfaces. *Annu. Rev. Phys. Chem.* **1989**, *40*, 327–350.
- (29) Abdelwahab, I.; Tilmann, B.; Wu, Y.; Giovanni, D.; Verzhbitskiy, I.; Zhu, M.; Berté, R.; Xuan, F.; Menezes, L. d. S.; Eda, G.; Sum, T. C.; Quek, S. Y.; Maier, S. A.; Loh, K. P. Giant second-harmonic generation in ferroelectric NbOI₂. *Nat. Photon.* **2022**, *16*, 644–650.
- (30) Lucking, M. C.; Beach, K.; Terrones, H. Large second harmonic generation in alloyed TMDs and boron nitride nanostructures. *Sci. Rep.* **2018**, *8*, 10118.
- (31) Shree, S.; Lagarde, D.; Lombez, L.; Robert, C.; Balocchi, A.; Watanabe, K.; Taniguchi, T.; Marie, X.; Gerber, I. C.; Glazov, M. M.; Golub, L. E.; Urbaszek, B.; Paradisanos, I. Interlayer exciton mediated second harmonic generation in bilayer MoS₂. *Nat. Commun.* **2021**, *12*, 6894.
- (32) Seyler, K. L.; Schaibley, J. R.; Gong, P.; Rivera, P.; Jones, A. M.; Wu, S.; Yan, J.; Mandrus, D. G.; Yao, W.; Xu, X. Electrical control of second-harmonic generation in a WSe₂ monolayer transistor. *Nat. Nanotechnol.* **2015**, *10*, 407–411.
- (33) Carvalho, B. R.; Wang, Y.; Fujisawa, K.; Zhang, T.; Kahn, E.; Bilgin, I.; Ajayan, P. M.; de Paula, A. M.; Pimenta, M. A.; Kar, S.; Crespi, V. H.; Terrones, M.; Malard, L. M. Nonlin-

- ear Dark-Field Imaging of One-Dimensional Defects in Monolayer Dichalcogenides. *Nano Lett.* **2020**, *20*, 284–291.
- (34) Malard, L. M.; Alencar, T. V.; Barboza, A. P. M.; Mak, K. F.; de Paula, A. M. Observation of intense second harmonic generation from MoS₂ atomic crystals. *Phys. Rev. B* **2013**, *87*, 201401.
- (35) Mennel, L.; Paur, M.; Mueller, T. Second harmonic generation in strained transition metal dichalcogenide monolayers: MoS₂, MoSe₂, WS₂, and WSe₂. *APL Photonics* **2018**, *4*, 034404.
- (36) Zuo, Y. et al. Optical fibres with embedded two-dimensional materials for ultrahigh nonlinearity. *Nat. Nanotechnol.* **2020**, *15*, 987–991.
- (37) Wang, G.; Chernikov, A.; Glazov, M. M.; Heinz, T. F.; Marie, X.; Amand, T.; Urbaszek, B. Colloquium: Excitons in atomically thin transition metal dichalcogenides. *Rev. Mod. Phys.* **2018**, *90*, 021001.
- (38) Mueller, T.; Malic, E. Exciton physics and device application of two-dimensional transition metal dichalcogenide semiconductors. *npj 2D Mater. Appl.* **2018**, *2*, 29.
- (39) Lafeta, L.; Corradi, A.; Zhang, T.; Kahn, E.; Bilgin, I.; Carvalho, B. R.; Kar, S.; Terrones, M.; Malard, L. M. Second- and third-order optical susceptibilities across exciton states in 2D monolayer transition metal dichalcogenides. *2D Mater.* **2021**, *8*, 035010.
- (40) Kumar, N.; Najmaei, S.; Cui, Q.; Ceballos, F.; Ajayan, P. M.; Lou, J.; Zhao, H. Second harmonic microscopy of monolayer MoS₂. *Phys. Rev. B* **2013**, *87*, 161403.
- (41) Pike, N. A.; Pachter, R. Angular Dependence of the Second-Order Nonlinear Optical Response in Janus Transition Metal Dichalcogenide Monolayers. *J. Phys. Chem. C* **2022**, *126*, 16243–16252.

- (42) He, K.; Kumar, N.; Zhao, L.; Wang, Z.; Mak, K. F.; Zhao, H.; Shan, J. Tightly Bound Excitons in Monolayer WSe₂. *Phys. Rev. Lett.* **2014**, *113*, 026803.
- (43) Ye, Z.; Cao, T.; O'Brien, K.; Zhu, H.; Yin, X.; Wang, Y.; Louie, S. G.; Zhang, X. Probing excitonic dark states in single-layer tungsten disulphide. *Nature* **2014**, *513*, 214–218.
- (44) Budde, H.; Coca-López, N.; Shi, X.; Ciesielski, R.; Lombardo, A.; Yoon, D.; Ferrari, A. C.; Hartschuh, A. Raman Radiation Patterns of Graphene. *ACS Nano* **2016**, *10*, 1756–1763.
- (45) Lieb, M. A.; Zavislan, J. M.; Novotny, L. Single-molecule orientations determined by direct emission pattern imaging. *J. Opt. Soc. Am. B* **2004**, *21*, 1210–1215.
- (46) Spychala, K. J.; Mackwitz, P.; Widhalm, A.; Berth, G.; Zrenner, A. Spatially resolved light field analysis of the second-harmonic signal of $\chi^{(2)}$ -materials in the tight focusing regime. *J. Appl. Phys.* **2020**, *127*, 023103.
- (47) Hecht, B.; Novotny, L. *Principles of Nano-Optics*, 2nd ed.; Cambridge University Press: Cambridge, 2012; pp 45–85.
- (48) Birkmeier, K.; Hartschuh, A. Wavelength-tunable ultrafast two arm fiber laser system for transient interferometric scattering microscopy on nanoscopic objects. *J. Opt. Soc. Am. B* **2024**, *41*, 493–499.
- (49) Novoselov, K. S.; Geim, A. K.; Morozov, S. V.; Jiang, D.; Zhang, Y.; Dubonos, S. V.; Grigorieva, I. V.; Firsov, A. A. Electric Field Effect in Atomically Thin Carbon Films. *Science* **2004**, *306*, 666–669.
- (50) Castellanos-Gomez, A.; Buscema, M.; Molenaar, R.; Singh, V.; Janssen, L.; van der Zant, H. S. J.; Steele, G. A. Deterministic transfer of two-dimensional materials by all-dry viscoelastic stamping. *2D Mater.* **2014**, *1*, 011002.

ACKNOWLEDGEMENTS

L. L. and L. M. acknowledge support from the Alexander von Humboldt Foundation. We acknowledge financial support from the Deutsche Forschungsgemeinschaft (DFG) through Germany's Excellence Strategy-EXC 2089/1-390776260.

AUTHOR CONTRIBUTIONS

All authors wrote and reviewed the manuscript.

COMPETING INTERESTS

The authors declare no competing interests.

SUPPLEMENTARY INFORMATION

Supplementary information accompanies this paper.

Supplementary Information: Probing Noncentrosymmetric 2D Materials by Fourier Space Second Harmonic Imaging

Lucas Lafeta,^{*,†} Sean Hartmann,[†] Bárbara Rosa,[‡] Stephan Reitzenstein,[‡]
Leandro M. Malard,^{*,¶} and Achim Hartschuh^{*,†}

[†]*Department of Chemistry and CeNS, LMU Munich, Butenandtstr. 5-13, 81377 Munich,
Germany.*

[‡]*Institute of Solid State Physics, Technische Universität Berlin, Hardenbergstraße 36, 10623
Berlin, Germany.*

[¶]*Departamento de Física, Universidade Federal de Minas Gerais, Av. Antônio Carlos 6627, Belo
Horizonte, Minas Gerais 30123-970, Brazil.*

E-mail: lucas.lafeta@cup.lmu.de; lmalard@fisica.ufmg.br; achim.hartschuh@lmu.de

Table of content

- Supplementary Note 1: Experimental setup
- Supplementary Note 2: Sample Characterization
- Supplementary Note 3: Model for Fourier space SHG in 2D materials
- Supplementary Note 4: Accuracy of crystal orientation determination
- Supplementary Note 5: Focus dependence of SHG images for azimuthal laser mode
- Supplementary References

Supplementary Note 1: Experimental setup

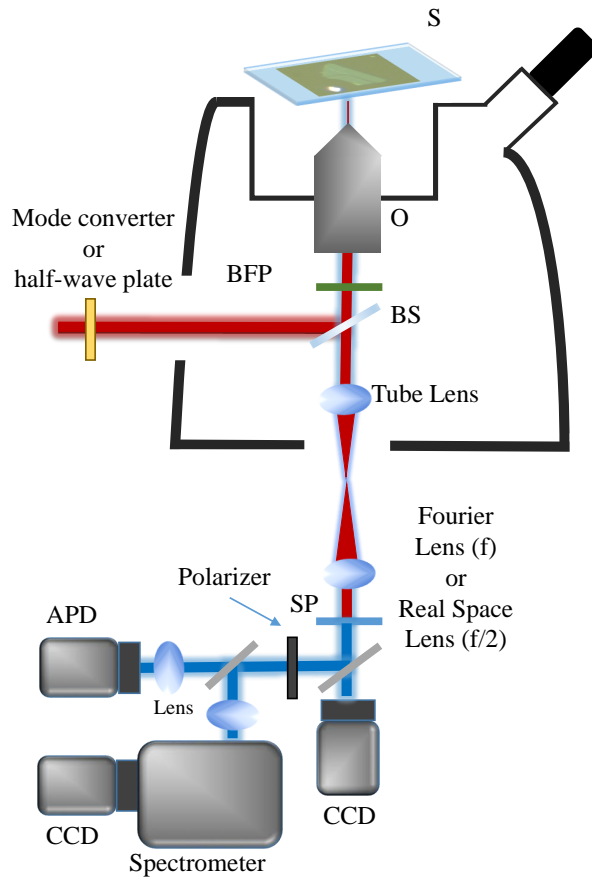


Figure 1: Illustration of the experimental setup: The setup consists of a femtosecond pulsed source operating at 880 nm.¹ The incident laser pulses (red) pass a half-wave plate (for Gaussian laser mode) or a mode converter (for azimuthal laser mode), are reflected by a beam splitter (BS) and focused by a microscope objective (O) (immersion oil objective, 100x, NA=1.3) on the sample (S). The sample response (SHG, 2PL) is detected in epi-configuration after passing the BS and a spectral short-pass filter (SP) to suppress scattered light at the laser wavelength. Fourier space images are recorded using a CCD camera in combination with a Fourier lens with focal length f positioned at a distance f from the focus of the tube lens and the CCD camera, respectively. Real space images are obtained by replacing the Fourier lens with a lens of $f/2$. A flip mirror is introduced to guide the light to a spectrometer equipped with a CCD or an avalanche photodiode (APD) for measuring spectra and confocal images. A polarizer is introduced to measure polarization resolved SHG.

Supplementary Note 2: Sample Characterization

All flakes were made by micromechanical exfoliation and encapsulated by transference using PDMS.^{2,3} The samples were characterized using optical wide-field imaging and Raman spectroscopy for h-BN and photoluminescence (PL) for MoSe₂ and WSe₂. SHG confocal maps were recorded for all samples. The characterization results show monolayers for TMDs and a few layers for h-BN, as illustrated in Figure 2.

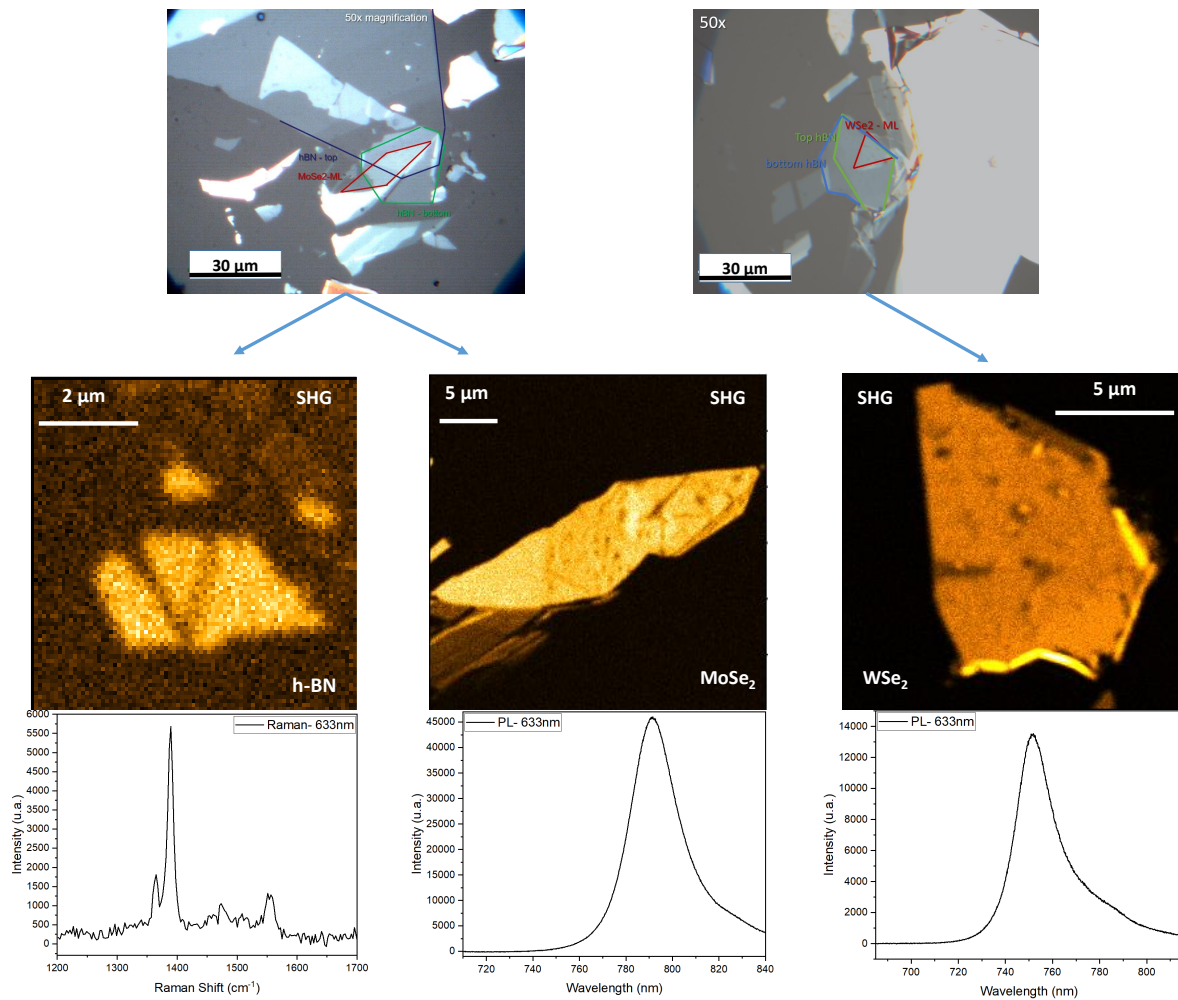


Figure 2: Sample characterization: Top: Bright-field contrast images of the encapsulated samples: MoSe₂ together with h-BN (left) and WSe₂ (right). Middle: Confocal SHG images were recorded using the APD for h-BN (left), MoSe₂ (middle), and WSe₂ (right). Bottom: Raman spectrum of the h-BN sample showing the E_{2g} mode characteristic of h-BN (left). Photoluminescence spectrum of MoSe₂ (middle) and WSe₂ (right) with the characteristic photoluminescence emission of monolayers.

Supplementary Note 3: Model for Fourier space SHG in 2D materials

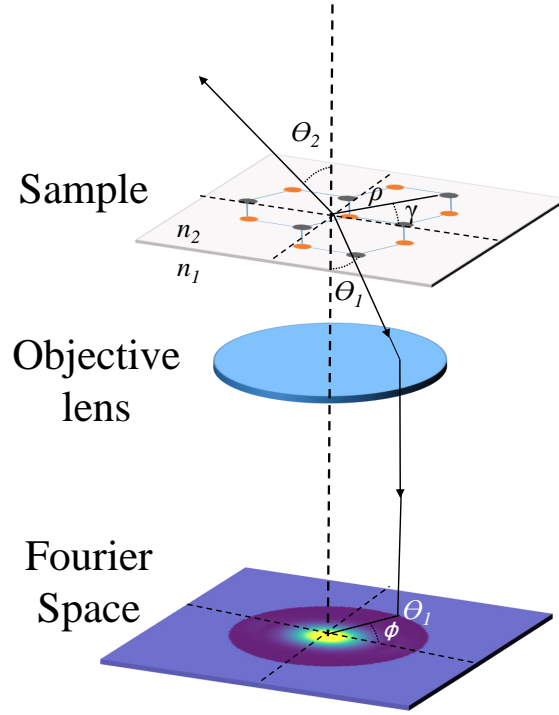


Figure 3: Illustration of the model used for calculating radiation patterns in Fourier space by back-focal plane (BFP) imaging.

Radiation patterns in Fourier space and real space images are calculated from the sum of the fields generated by coherent dipoles within the 2D material layer oscillating at 2ω using a Python script. The strength of these dipoles is scaled with the local electric field of the exciting laser in the focus of the microscope objective.^{4,5} In the following, we define the parameters used in the available Python script.

1. Parameters

- n_1 (n_2) Refractive index in the lower halfspace formed by the substrate (upper halfspace)
- θ_1 (θ_2) Collection angle in the lower halfspace (upper halfspace)
- $\lambda_{ex}(lex)$ Wavelength of the excitation light
- $\lambda(l)$ Wavelength of the SH light ($k_i = 2\pi n_i/\lambda$)

- NA Numerical aperture of the microscope objective
- ff Filling factor of the microscope objective
- ϕ Polar angle in the BFP
- γ Polar angle in the real space focal plane ($\gamma = \arctan(y, x)$), ρ radius ($\rho = \sqrt{x^2 + y^2}$)

2. Fresnel coefficients for air-TMD-glass interface

$$r_p = \frac{n_1 \cos \theta_2 - n_2 \cos \theta_1 + Z_0 \sigma \cos \theta_1 \cos \theta_2}{n_1 \cos \theta_2 - n_2 \cos \theta_1 + Z_0 \sigma \cos \theta_1 \cos \theta_2}, t_p = (1 - r_p) \frac{\cos \theta_2}{\cos \theta_1} \quad (1)$$

$$r_s = \frac{n_2 \cos \theta_2 - n_1 \cos \theta_1 - Z_0 \sigma}{n_2 \cos \theta_2 + n_1 \cos \theta_1 + Z_0 \sigma}, t_s = r_s + 1 \quad (2)$$

3. Calculation of focal excitation field ⁴

Apodization function:

$$f_w(\theta_1) = \exp(-n_1/ff \sin \theta_1/NA) \quad (3)$$

Angular integrals:

$$I_{00} = \int f_w(\theta_1) \sqrt{\cos \theta_1} \sin \theta_1 (1 + \cos \theta_1) J_0(k_1 \rho \sin \theta_1) d\theta_1 \quad (4)$$

$$I_{02} = \int f_w(\theta_1) \sqrt{\cos \theta_1} \sin \theta_1 (1 - \cos \theta_1) J_2(k_1 \rho \sin \theta_1) d\theta_1 \quad (5)$$

$$I_{11} = \int f_w(\theta_1) \sqrt{\cos \theta_1} \sin^2 \theta_1 (1 + 3 \cos \theta_1) J_1(k_1 \rho \sin \theta_1) d\theta_1 \quad (6)$$

$$I_{12} = \int f_w(\theta_1) \sqrt{\cos \theta_1} \sin^2 \theta_1 (1 - \cos \theta_1) J_1(k_1 \rho \sin \theta_1) d\theta_1 \quad (7)$$

In-plane focal field components, oriented along α with respect to crystal axis:

1. Linearly polarized Gaussian mode

$$E_x(\rho, \gamma) = I_{00}(\rho) + I_{02}(\rho) \cos(2(\gamma - \alpha)), E_y(\rho, \gamma) = I_{02}(\rho) \sin(2(\gamma - \alpha)) \quad (8)$$

2. Azimuthally polarized doughnut mode

$$E_x(\rho, \gamma) = i(I_{11}(\rho) + 3I_{12}(\rho)) \sin(\gamma - \alpha), E_y(\rho, \gamma) = -i(I_{11}(\rho) + 3I_{12}(\rho)) \cos(\gamma - \alpha) \quad (9)$$

Projected on to crystal axis:

$$E_{x,c}(\rho, \gamma) = \cos \alpha E_x - \sin \alpha E_y, E_{y,c}(\rho, \gamma) = \sin \alpha E_x + \cos \alpha E_y \quad (10)$$

4. SHG

$$P_{x,c}^{2\omega}(\rho, \gamma) = 2E_{x,c}E_{y,c}, P_{y,c}^{2\omega}(\rho, \gamma) = E_{x,c}^2 - E_{y,c}^2 \quad (11)$$

5. Radiation pattern ⁴

Emission coefficients:

$$c_2 = \frac{n_1}{n_2} t_p, c_3 = -\frac{n_1 \cos \theta_1}{n_2 \cos \theta_2} t_s \quad (12)$$

p- and s-polarized fields emitted by single point dipole:

$$E_p^{2\omega}(\rho, \gamma; \theta_1, \phi) = c_2 \cos \theta_1 (\cos \phi P_{x,c} + \sin \phi P_{y,c}), E_s^{2\omega}(\rho, \gamma; \theta_1, \phi) = c_3 (\sin \phi P_{x,c} - \cos \phi P_{y,c}) \quad (13)$$

Components in x- and y-direction:

$$E_x^{2\omega}(\rho, \gamma; \theta_1, \phi) = \cos \phi E_p - \sin \phi E_s, E_y^{2\omega}(\rho, \gamma; \theta_1, \phi) = \sin \phi E_p + \cos \phi E_s \quad (14)$$

Propagation phase factor for dipoles at (x, y)

$$p_f(x, y; \theta_1, \phi) = \exp(-ik_1(x \cos \phi \sin \theta_1 + y \sin \phi \sin \theta_1)) \quad (15)$$

Total field in the BFP from the coherent sum of dipole field :

$$E_{x,total}^{2\omega}(\theta_1, \phi) = \int E_x^{2\omega}(x, y; \theta_1, \phi) p_f dx dy, E_{y,total}^{2\omega}(\theta_1, \phi) = \int E_y^{2\omega}(x, y; \theta_1, \phi) p_f dx dy \quad (16)$$

Detected Fourier SHG patterns in BFP with $k_x/k_0 = n_1 \sin \theta_1 \cos \phi$ and $k_y/k_0 = n_1 \sin \theta_1 \sin \phi$:

$$I^{2\omega}(\theta_1, \phi) = \frac{1}{\cos \theta_1} (|E_{x,total}^{2\omega}|^2 + |E_{y,total}^{2\omega}|^2) \quad (17)$$

2PL Fourier patterns are calculated from the incoherent sum of the intensity BFP patterns of two orthogonal in-plane dipoles with equal strength.⁶

Real space images are calculated by further propagating these fields followed by focusing.⁴

Supplementary Note 4: Accuracy of crystal orientation determination

We determined the accuracy of the crystal orientation determination using Fourier SHG imaging for azimuthal mode excitation after rotating the sample by different angles and comparing the derived values with those observed in real space optical images. In Fig. 4, we recorded wide-field optical images (a, e) and the corresponding confocal SHG maps (b, f). We measured the angle between the indicated sample edge relative to 0° (horizontal yellow line). The angles were determined using the ImageJ software (see Table 1). Afterwards, we detected the Fourier SHG images using the azimuthal mode (c, g). Then, we made a polar plot of the SHG intensity along the red circle in the images in Fig. 4 c, g. These plots are shown in Fig. 4 d, h, and were fitted (red curves in d, h) using the following equation:⁷

$$I^{SHG}(\phi) = (A \sin 3(\phi + P))^2 + C \quad (18)$$

Here, A is the SHG amplitude, P represents the angular orientation, and C is a small uniform background. The relative angular orientation extracted from the fit demonstrates a higher accuracy than the direct determination using ImageJ (see Fig. 4). In Table 1 below, we show the angles extracted from ImageJ for the sample of MoSe_2 measured by wide-field illumination, the same sample under the same conditions mapped by confocal SHG imaging, and the values extracted from the fit to the polar plot of the Fourier SHG data. The uncertainty of this fit is ± 0.5 as given by its standard deviation. The last row lists the angular difference between the sample in position Fig. 4 a and Fig. 4 e (a-e) determined by the different techniques.

Table 1: Orientation angles obtained from different techniques for MoSe_2 .

MoSe_2	Wide-field	SHG Map	Fourier SHG azimuthal mode
a, b, c	102.0°	102.3°	102.2°
e, f, g	9.9°	8.3°	9.2°
a - e	92.1°	94.0°	93.0°

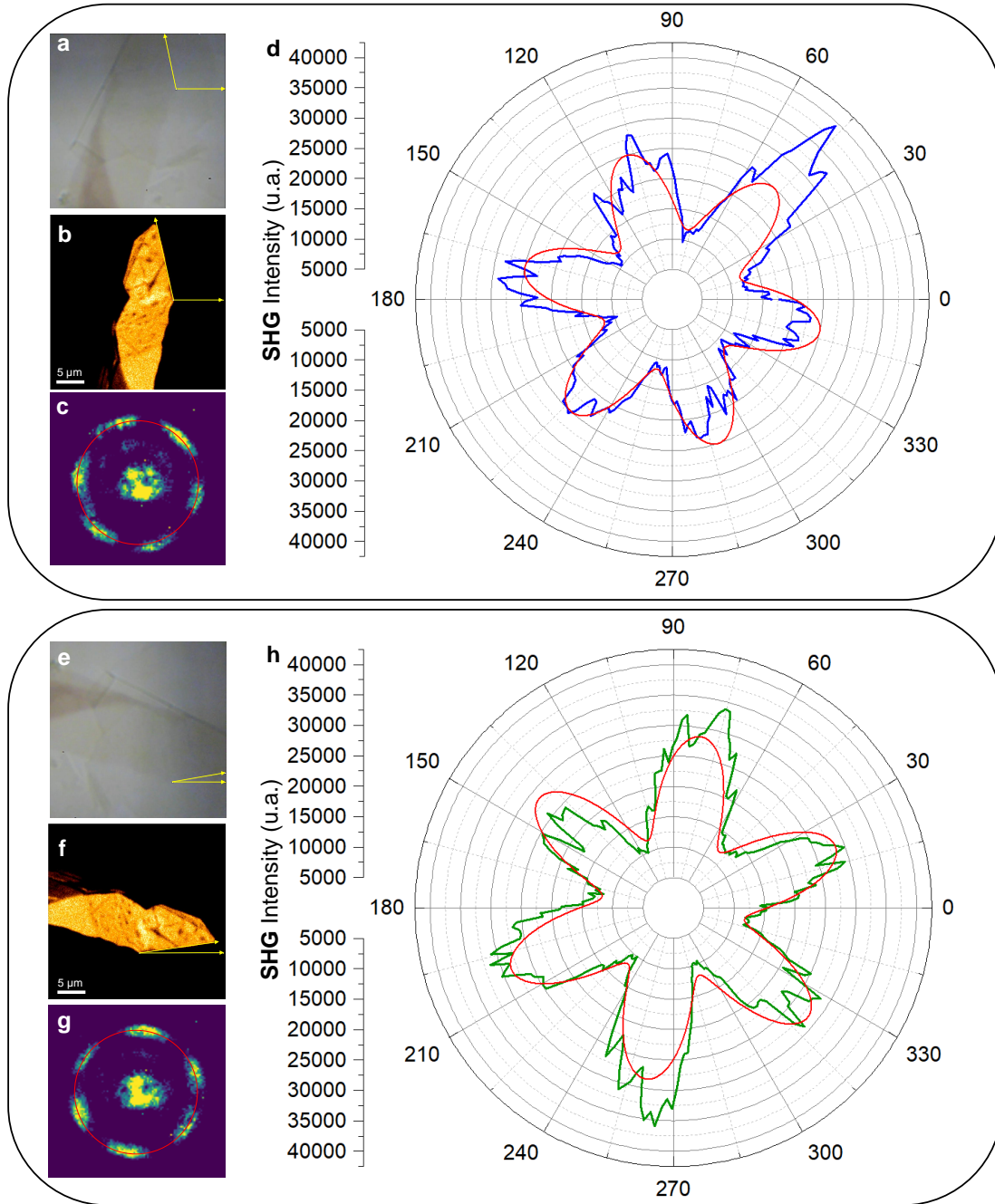


Figure 4: Measurement of a MoSe₂ monolayer in two different in-plane orientations. **a,e** Wide-field optical images with the orientational angle determined by ImageJ. **b,f** Confocal SHG maps measured using the APD with the angles determined by ImageJ. **c, g** Fourier space SHG images using the azimuthal mode and **d,h** polar plots together with fits of the red circle from image **c, g** using eqn.18.

To confirm the accuracy of the Fourier SHG technique, we measured a different sample (WSe₂) rotated by small angles, as shown in Fig. 5. The values obtained in the experiment of Fig. 5 are

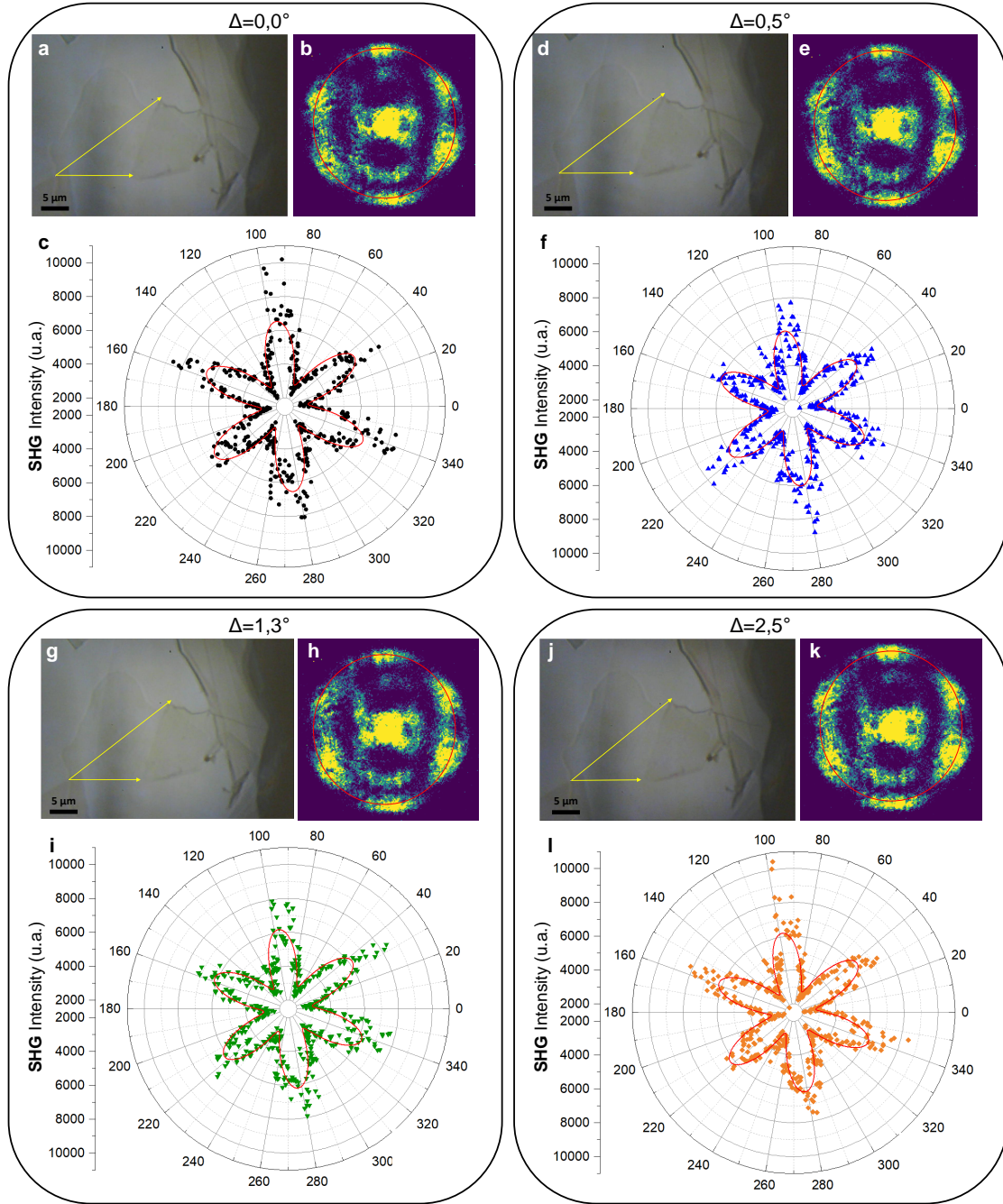


Figure 5: Measurement of a WSe_2 monolayer after rotation by small angles. **a, d, g, j** wide-field images, the angle of the monolayer was determined by ImageJ. **b, e, h, k**, Fourier SHG imaging was done using the azimuthal mode. **c, f, i, l** polar plots of the red circles from **b, e, h, k** together with the fits using eqn. 18.

presented in Table 2. The table lists the changes in angular orientation Δ relative to the first orientation seen in Fig. 5 a, b, c.

Table 2: Changes in orientation angle obtained from different techniques for WSe₂.

MoSe ₂	Δ (Wide-field)	Δ (Fourier SHG azimuthal mode)
a, b, c	0.0°	0.0°
d, e, f	0.6°	0.5°
g, h, i	1.3°	1.3°
j, k, l	2.3°	2.5°

Supplementary Note 5: Focus dependence of SHG images for azimuthal laser mode

Using the model described in the main manuscript and in Supplementary Note 3, we can simulate Fourier and real space images for the azimuthally polarized laser mode for different defocus conditions. Upon defocusing, the Fourier SHG images retain their 6-fold symmetry and orientation (Fig. 6), as can be seen in both calculated and experimental patterns. Whereas the real space images always display 6-fold patterns, their orientation changes upon defocusing. In focus, the real space image shows a hexagonal pattern that is rotated with respect to the Fourier space pattern by 30° . Fourier space SHG detection thus provides a robust way to visualize the crystal orientation.

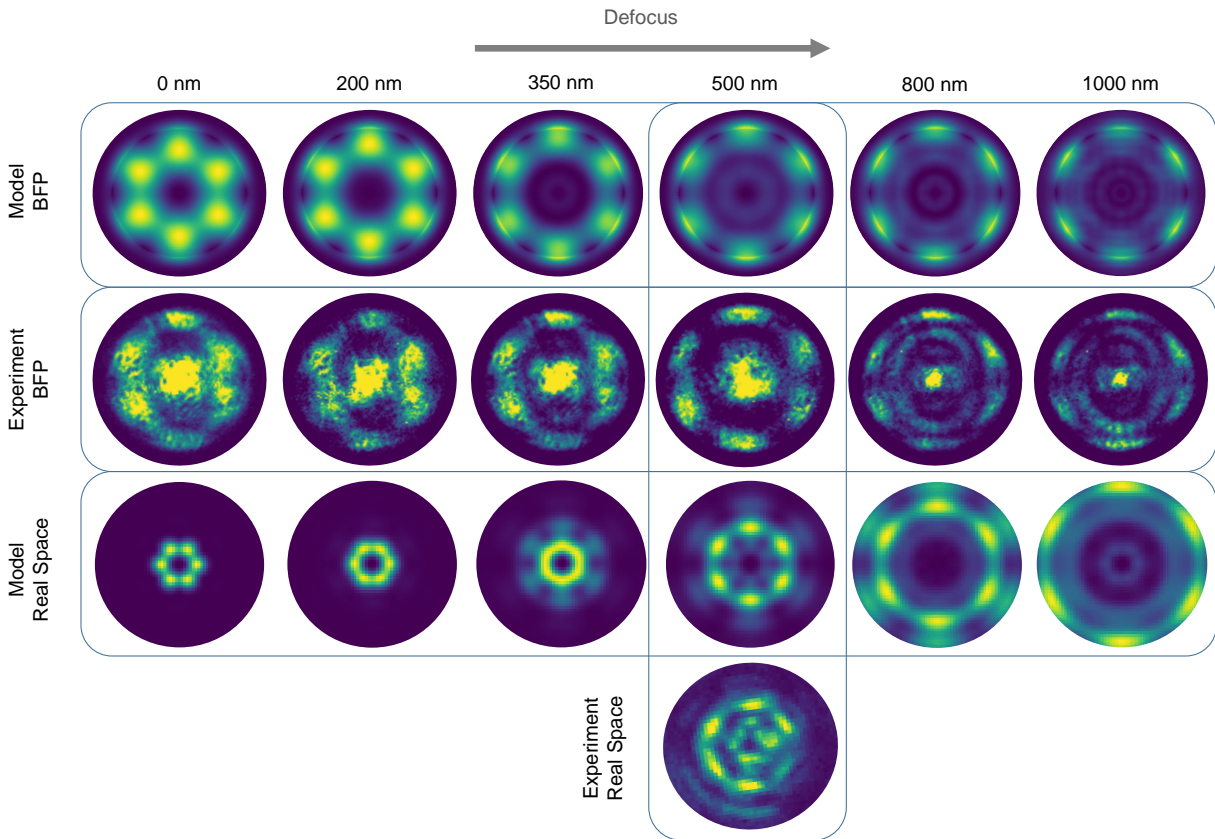


Figure 6: Focus dependence of calculated and experimental SHG images of MoSe_2 for an azimuthally polarized laser mode. Upper two rows: Fourier space BFP patterns. Lower two rows: Corresponding real space patterns.

REFERENCES

- (1) Birkmeier, K.; Hartschuh, A. Wavelength-tunable ultrafast two arm fiber laser system for transient interferometric scattering microscopy on nanoscopic objects. *J. Opt. Soc. Am. B* **2024**, *41*, 493–499.
- (2) Mennel, L.; Paur, M.; Mueller, T. Second harmonic generation in strained transition metal dichalcogenide monolayers: MoS₂, MoSe₂, WS₂, and WSe₂. *APL Photonics* **2018**, *4*, 034404.
- (3) Castellanos-Gomez, A.; Buscema, M.; Molenaar, R.; Singh, V.; Janssen, L.; van der Zant, H. S. J.; Steele, G. A. Deterministic transfer of two-dimensional materials by all-dry viscoelastic stamping. *2D Mater.* **2014**, *1*, 011002.
- (4) Hecht, B.; Novotny, L. *Principles of Nano-Optics*, 2nd ed.; Cambridge University Press: Cambridge, 2012; pp 45–85.
- (5) Lieb, M. A.; Zavislan, J. M.; Novotny, L. Single-molecule orientations determined by direct emission pattern imaging. *J. Opt. Soc. Am. B* **2004**, *21*, 1210–1215.
- (6) Budde, H.; Coca-López, N.; Shi, X.; Ciesielski, R.; Lombardo, A.; Yoon, D.; Ferrari, A. C.; Hartschuh, A. Raman Radiation Patterns of Graphene. *ACS Nano* **2016**, *10*, 1756–1763.
- (7) Malard, L. M.; Alencar, T. V.; Barboza, A. P. M.; Mak, K. F.; de Paula, A. M. Observation of intense second harmonic generation from MoS₂ atomic crystals. *Phys. Rev. B* **2013**, *87*, 201401.